HHS Public Access

Author manuscript

Nano Lett. Author manuscript; available in PMC 2019 November 14.

Published in final edited form as:

Nano Lett. 2018 November 14; 18(11): 7092–7103. doi:10.1021/acs.nanolett.8b03096.

Unique photo-chemo-immuno-nanoplatform against orthotopic xenograft oral cancer and metastatic syngeneic breast cancer

Lu Zhang[†,#], **Di Jing**[†,⊥,#], **Lei Wang**[‡], **Yuan Sun**[†], **Jian Jian Li**[‖], **Brianna Hill**[†], **Fan Yang**[†], **Yuanpei Li**[†,*], and **Kit S Lam**[†,*]

[†]Department of Biochemistry and Molecular Medicine, UC Davis NCI-designated Comprehensive Cancer Center, University of California Davis, Sacramento, California, 95817, USA.

[‡]CAS Center for Excellence in Nanoscience, CAS Key Laboratory for Biomedical Effects of Nanomaterials and Nanosafety, National Center for Nanoscience and Technology, Beijing 100190, China.

[‖]Director of Translational Research, Department of Radiation Oncology, School of Medicine, University of California Davis, Sacramento, California, 95817, USA.

[⊥]Department of Oncology, Xiangya Hospital, Central South University, Hunan, 410008, China.

Abstract

Sophisticated self-assembly may endow materials with a variety of unique functions that are highly desirable for therapeutic nanoplatform. Herein, we report the co-assembly of two structurally-defined telodendrimers, each comprised of hydrophilic linear PEG and hydrophobic cholic acid cluster as a basic amphiphilic molecular subunit. One telodendrimer has four added indocyanine green derivatives, leading to excellent photothermal properties; the other telodendrimer has four sulfhydryl groups designed for efficient inter-subunit cross-linking, contributing to superior stability during circulation. The co-assembled nanoparticle (CPCI-NP) possesses superior photothermal conversion efficiency as well as efficient encapsulation and controlled release of cytotoxic molecules and immunomodulatory agents. CPCI-NP loaded with doxorubicin has proven to be a highly efficacious combination photothermal/chemo-therapeutic nanoplatform against orthotopic OSC-3 oral cancer xenograft model. When loaded with imiquimod, a potent small molecule immunostimulant, CPCI-NP was found to be highly effective against 4T1 syngeneic murine breast cancer model, particularly when photothermal/immuno-therapy is given in combination with PD-1 checkpoint blockade antibody. Such triple therapy not

[*]**Corresponding Authors** kslam@ucdavis.edu. Tel: (916)7340910. [*] lypli@ucdavis.edu. Tel: (916)7344420. Fax: (916)7346415.
[#]L.Z. and D.J. contributed equally to this work.

Supporting Information

The Supporting Information is available free of charge on the ACS Publications website at DOI: 10.1021/acs.nanolett.8b03096
Additional details on experimental materials and methods. Figures showing synthetic approach of ICGD, chemical characterization of ICGD molecule and PCI/PCLC telodendrimer, fluorescence spectra, photothermal conversion behavior, the encapsulation efficiency of DOX and imiquimod, detection of apoptotic OSC-3 oral cells using flow cytometry assay, blood test parameters, body weight curves of mice bearing orthotopic OSC-3 oral cancer, cumulative survival of mice bearing 4T1 breast cancer. H&E staining of tumor slices, IHC staining for $CD8^+$, $CD3^+$, $CD4^+$, PD-1, PD-L1, MHC II and CD11b in both sides 4T1 tumor tissue, immune memory effect of synergistic photothermal-/immunotherapy. Table showing pharmacokinetics parameter in rats received CPCI-NP, PCLC/TBAI&ICG-NP and free ICG. (PDF)

Notes

The authors declare no competing interests.

only eradicates the light-irradiated primary tumors, but also activates systemic anti-tumor immunoactivity, causing tumor death at light-unexposed distant tumor sites. This co-assembled multi-functional, versatile, and easily scalable photothermal immuno-nanoplatform shows great promise for clinical translation.

Graphical Abstract

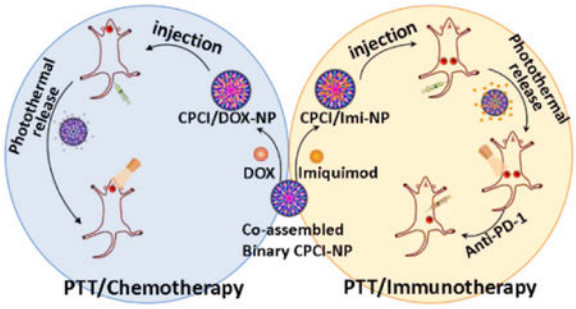

Keywords

binary telodendrimer; photothermal nanocarrier; nano-photo-immunotherapy; nano-photo-chemotherapy; orthotopic oral cancer; metastatic breast cancer

Many near-infrared photothermal conversion agents (PTCAs) are being developed for cancer photothermal therapy (PTT), most of which are still in the preclinical stage.[1-8] The vast majority of these agents still face significant challenges in clinical translation. These include low photothermal conversion efficiency, poor biocompatibility (*e.g.* inorganic nanoagents) and poor *in vivo* stability (rapid clearance from kidney or liver *in vivo* and poor resistance to photo-bleaching, *e.g.* small-molecule dyes). Photothermal conversion efficiency can be increased by using nanomaterial that absorbs at infrared, with wavelength >800 nm. Near-infrared light can penetrate deeper into the tissue, limit interference with blood and tissue, and cause less photodamage to normal tissues. Another approach to increase photothermal conversion efficiency is to increase the gather density/structure and optical-absorption cross-section of PTCAs at the target tumor sites.[9]

There have been many recent reports on using biocompatible nanomaterials to physically encapsulate organic small molecule PTCAs such as porphyrin, Ce6 or indocyanine green (ICG) to improve the pharmacokinetics and tumor targeting efficiency of these small-molecule dyes.[10, 11] However, the photothermal conversion efficiency for this class of photothermal materials is low because of short excitation wavelength (*e.g.* 690 nm for porphyrin or Ce6) and therefore low tissue penetration. In addition, leakage of small molecule dyes from the nanocarriers during circulation is problematic. One approach to overcome the circulation leak and improve photostability is to covalently conjugated the dyes to the polymers and macromolecules.[12, 13]

Clinical applications of PTT are generally limited to the treatment of localized tumors that are accessible to light irradiation. It also has potential to be used intraoperatively to treat the tumor bed when patients' tumor sites are exposed during surgery. Concurrent chemotherapy

in combination with PTT has been shown to be synergistic.[14-17] Therefore it is advantageous for the PTCA to have high capacity to encapsulate cytotoxic agents. A few years ago, we reported the development of an amphiphilic hybrid telodendrimer, comprised of linear PEG linked to cluster of cholic acid and pyropheophorbide-a, a porphyrin derivative, which could self-assemble to form micellar nanoporphyrin with favorable photothermal (absorption at 690nm) and pharmacokinetic properties.[2, 18]

Majority of cancer deaths, however, are caused by metastases. In fact the majority of solid tumors are no longer curable once metastasis has occurred. In the last few years, there is great excitement in the use of check point blockade antibodies (*e.g.* anti-PD-1 monoclonal antibody) for cancer immunotherapy.[10, 19-27] Durable clinical responses have been seen in patients with advanced diseases. Although the response rate for patients with melanoma and non-small cell lung cancers has reached 25-40%, it is much lower (<10%) for most other cancers, and the treatment has only benefited patients whose tumors have been pre-infiltrated with T cells. There is great need to develop therapeutic approaches that can increase the response rate as well as the tumor spectrum responsive to check point blockade immunotherapy.[28-36] In addition to combining more than one check point blockade antibody (e.g. anti-PD-1 plus anti-CTLA4), many other additional modalities are being investigated. For example, PTT has been shown to not only kill tumor cells directly *via* induction of apoptosis and necrosis, but it could also generate anti-tumor immunological responses to improve systemic immunotherapeutic effect by generating tumor-associate antigens from ablated tumor cell residues. Delivery of potent immunostimulants to tumor sites causing an increase in tumor infiltrating T-cells may augment the overall anti-tumor immune response.

Here we report on a novel photothermal conversion nanoplatform capable of (1) loading cytotoxic agents such as doxorubicin, for highly efficacious combination photothermal-chemotherapy against orthotopic oral cancer xenograft, and (2) encapsulating imiquimod[37], a potent small molecule immuno-stimulator that can greatly augment PD-1 checkpoint blockade immunotherapy in a syngeneic breast cancer model (Schema 1). This photothermal nanoplatform is formed by co-assembly of two distinct telodendrimers, each with unique functions. The first hybrid telodendrimer (PEG^{5K}-CA_4-$ICGD_4$, aka PCI) is comprised of a linear PEG block, four dendritic hydrophobic photothermal conversion agents (indocyanine green derivatives, ICGD) and four dendritic cholic acids (CA). The second telodendrimer (PEG^{5K}-Cys_4-L_8-CA_8, aka PCLC) comprised of PEG, four cysteines and eight CA, can co-assemble with PCI at 1:1 ratio to form a highly stable disulfide cross-linked versatile micellar nanosystem (CPCI-NP, Figure 1a) with high photothermal conversion efficiency. The design of this nanoplatform is based on our previously reported micellar nanoporphyrin[2, 18], in which pyropheophorbide-a, a derivative of porphyrin instead of ICGD, was used as the photoactive building block. ICGD was chosen here because ICGD absorbs at longer wavelength (808 nm) than porphyrin (690 nm). As a result, the photothermal and photodynamic property of CPCI-NP is superior to that of nanoporphyrin. Furthermore, ICG has been used as optical tracer in the clinics for decades, and its emission wavelength is longer than that of porphyrin. CPCI-NP is therefore an excellent probe for image-guided surgery and intraoperative phototherapy against cancer. Similar to nanoporphyrin, drug-loading property and final particle size of CPCI-NP are favorable for drug delivery. Most importantly, we have been able to demonstrate that CPCI-NP loaded

with imiquimod, an immunostimulant, is able to greatly augment the efficacy of check point blockade antibodies. This attribute has yet to be explored with nanoporphyrin.

To impart the photothermal feature, ICGD was first synthesized (Figure S1). As shown in Figure S2, ^{1}NMR and ESI mass spectrometry verified the chemical structures of ICGD. ICGD molecule was functionalized with a carboxylic acid group, so that four ICGD units could be easily grafted to obtain PCI telodendrimer with molecular weight 10,430 Da (Figure S3a-c). The absorption (two peaks around 720 nm and 795 nm) and fluorescence emission (a peak value of 835 nm) of PCI telodendrimer and single ICGD molecule in methanol were almost identical, indicating the successful introduction of ICGD into PCI (Figure S3d,e). Given its hydrophobicity and tendency for π-π interactions, dendritic ICGD and CA in amphiphilic PCI telodendrimer could easily self-assemble into thermodynamically stable nanoparticles (PCI-NP) with highly ordered structure and uniform size (~ 30 nm), which was simultaneously verified by dynamic light scattering (DLS) measurement and transmission electron micrograph (TEM) (Figure 1b). To improve the *in vivo* stability and photothermal conversion efficiency of PCI-NP, PCLC telodendrimer (Mn ≈ 12000, Figure S4) was introduced to form hybrid CPCI-NP. Thiol groups on the cysteines could form disulfide bonds inside the hydrophobic core of NPs under oxidative environment, contributing to the stability of NPs during circulation where lipoproteins are abundant.[38] Under this compositional design, the size of the CPCI-NP was smaller than that of PCI-NP, *i.e.* 20 ± 6 nm vs. 30 ± 8 nm (Figure 1c). This is a desirable particle size for efficient accumulation inside tumor by an enhanced permeability and retention (EPR) effect.

The stability of PCI-NP and CPCI-NP were tested in the presence of a strong ionic detergent sodium dodecyl sulfate (SDS) and an intracellular reductive glutathione (GSH).[39] As shown in Figure 1d, the immediate disappearance (<10 s) of particle size signal of PCI-NP reflected the distinct dynamic association-dissociation property of non-cross-linked PCI-NP. In sharp contrast, the particle size of CPCI-NP remained at around 20 nm in the presence of SDS (2.5 mg mL^{-1} final concentration), indicating high stability of such cross-linked NPs. Furthermore, in the presence of SDS and GSH (~ 10 mM), particle size signal of CPCI-NP rapidly disappeared, indicating that dissociation of CPCI-NP. Similar to PCI-NP, the fluorescence of ICGD in CPCI-NP PBS solution was also highly quenched. However, in the presence of both SDS and GSH, the fluorescence intensity of CPCI-NP solution was enhanced a 100 fold, which is consistent with our notion that ICGD self-assembled into highly-ordered structures (Figure S5a,b).

We further evaluated the photothermal conversion property *via* quantitative measurement of the temperature variations of CPCI-NP and PCI-NP in PBS solution under laser irradiation. As shown in Figure 1e, both CPCI-NP and PCI-NP solutions with equal ICGD content displayed rapid temperature increase in the first 60 *s*, *i.e.* 64.5 °C *vs.* 56.6 °C. After continuous laser irradiation for 300 s, the solution temperatures reached a plateau of about 78.5 °C and 68 °C for CPCI-NP and PCI-NP. In addition, the maximum temperature reached by gold nanorods (GNRs) was 51.2 °C, very similar result for other gold nanostructures reported in the literature (Figure S5d).[9, 12, 40] Using the previously reported method[12, 41], the photothermal conversion efficiency (η) of CPCI-NP at 808 nm was calculated to be 30.6 %, which is higher than that of PCI-NP (24.3%) and GNRs (18.1%).[3, 12] The photothermal

stability of CPCI-NP and PCI-NP were also studied by alternate heating and cooling cycles, in comparison with ICG.[42] As expected, photobleaching occurred rapidly in free ICG solution after repeated laser irradiation. CPCI-NP was found to maintain robust photothermal efficiency after laser irradiation (five cycles), and much higher plateau temperature and faster temperature rising rate comparing to PCI-NP (Figure 1f). Interestingly, when CPCI-NP was dissociated with GSH and SDS, repeated laser irradiation led to successive decrease in photothermal efficiency, suggesting that photobleaching protection in CPCI-NP was due to micellar configuration and not dendrimeric configuration of cyanine dyes. These high photothermal conversion efficiency and high stability of CPCI-NP could be originated from dense assembly of ICGD with strong π-π interaction.

To further study the high photothermal conversion efficiency of NPs, we investigated the variation of fluorescence intensity and photothermal conversion temperature at different concentrations of CPCI-NP in the form of assembly and disintegration. As shown in Figure 1g, photothermal conversion measurement demonstrated exact opposite properties with fluorescence intensity, *i.e.* high photothermal conversion efficiency in micellar form and low photothermal conversion efficiency in dissociated form. Compact configuration of ICGD in micellar CPCI-NP resulted in efficient generation of heat under laser irradiation at 808 nm. On the other hand, what is noteworthy is that the fluorescence intensity of CPCI-NP in PBS was weaker than that of PCI-NP (*e.g.* 320 *vs.* 800 at PCI concentration of 10 μM), while the photothermal conversion efficiency (temperature) was higher than that of PCI-NP (*e.g.* 69.6 °C *vs.* 58.2 °C at PCI concentration of 10 μM), indicating that configuration of ICGD in CPCI-NP was able to more efficiently convert excitation state energy into thermal energy rather than fluorescence (Figure S6). These results revealed that stable and compact micellar structure play a crucial role in photothermal conversion of PTCAs.

Given that our CPCI-NP is intended to be used *in vivo*, the relationship between tissue depth and temperature of CPCI-NP under laser irradiation at 808 nm was determined *in vitro* using 2 mm thick beef slice stack as the surrogate tissue barrier for light. Traditional ICG after complexing with TBAI was physically encapsulated into PCLC telodendrimer as a control.[43] As shown in Figure 1h,i, solution temperature of CPCI-NP and PCLC/TBAI&ICG-NP groups under 0.8 W cm^{-2} laser irradiation for 30 s through 2 mm beef slice can reach 70 °C and 50 °C, respectively. The temperature of PCLC/TBAI&ICG-NP was found to decrease to less than 40 °C when beef thickness was increased to 4 mm. In contrast, the temperature of CPCI-NP was able to reach around 45 °C even with the beef thickness increased to 6 mm. Since thickness of normal human skin and facial skin is generally less than 4 mm and 2 mm respectively, photothermal treatment with CPCI-NP could potentially be used to treat primary skin cancers. For comparison, we also investigated the photothermal effects of nanoporphyrin (based on our previous PEG^{5K}-$Porphyrin_4$-CA_4 telodendrimer[2], absorption wavelength: 690 nm, shorter than that of ICG) with respect to tissue depth. As expected, CPCI-NP was found to exhibit better heating efficiency and penetration depth when compared to nanoporphyrin (Figure S7). The superior performance of this photothermal nanosystem can be attributed to its high NIR absorbance, outstanding photothermal conversion efficiency, faster heating capability, and excellent photostability.

Based on our experience in telodendrimer-based micellar nanocarrier, we expect CPCI-NP to be an excellent carrier for chemotherapeutic drug DOX (Figure 2a).[2] As shown in Figure S8, when DOX concentration was raised to 3 mg mL^{-1}, the encapsulation efficiency was still above 70%, with a particle size remained at ~ 20 nm, confirming the excellent drug loading capacity of CPCI-NP. CPCI/DOX-NP also showed good serum stability in aqueous solution at 37 °C over the experimental period of 96 h (Figure 2b). Correspondingly, DOX could be controllably released from CPCI/DOX-NP with exogenous stimuli. As shown in Figure 2c, because fluorescence quenching of encapsulated DOX molecules, CPCI/DOX-NP PBS solution showed very weak fluorescence signal of DOX. However, the fluorescent intensity of DOX significantly enhanced when CPCI/DOX-NP was perturbed with laser irradiation in the presence of GSH (~ 10 mM). Similar results were shown in quantitative DOX release experiments. Without GSH and laser irradiation, DOX release rate in PBS was very slow (5.1% after 4 h, and less than 11% after 24 h). It was worth noting that DOX release could be dramatically increased at all times upon laser irradiation, and the total releasing amount of DOX could be further increased to 55% after 24 h, when CPCI/DOX-NP was exposed to GSH and sequential laser irradiation (Figure 2d). The enhanced release of DOX is probably due to the cleavage of S-S bonds at reducing environment with GSH plus local hyperthermia induced by photothermal conversion with laser, which could accelerate the diffusion of DOX out from crosslinked NPs. On-demand GSH (or N-acetyl cysteine[44, 45])-induced and photo-responsive drug release can be exploited *in vivo* to reduce the side effects of chemotherapeutics to normal tissues and enhance the cytotoxic effects at the tumor sites, after significant portion of CPCI/DOX-NP has reached the tumor sites.

Cellular uptake and intracellular distribution of CPCI/DOX-NP were evaluated by confocal laser scanning microscopy (CLSM) in OSC-3 oral cancer cells. As shown in Figure 2e, majority of the fluorescence signal from ICGD remained in the cytoplasm after 6 h of incubation. In contrast, DOX fluorescence was observed in both the cytoplasm and nucleus. This result suggested that the CPCI/DOX-NP was rapidly taken up by cancer cells, followed by release of portions of encapsulated DOX that ended up intercalating the DNA inside the nucleus. The synergistic chemo/photothermal therapy effect of CPCI/DOX-NP was evaluated on OSC-3 cells by a MTS assay. As shown in Figure 2f, CPCI-NP without laser group exhibited mild toxicity at the concentration of 200 μg mL^{-1} after incubation for 12 h. However, when the cells were irradiated by laser (808 nm, 0.8 W cm^{-2}, 2 min), the viability decreased significantly with the CPCI-NP concentration increased (< 5%; 200 μg mL^{-1}).

The chemo/photothermal synergistic therapy effect was further studied by using 50 μg mL^{-1} concentrations of CPCI-NP. For CPCI/DOX-NP alone at this lower concentration, only 32% cells were killed in the absence of laser exposure. However, more than 87% cells were killed for CPCI/DOX-NP plus laser irradiation group, which suggested great synergistic anti-tumor effect (Figure 2g). The live cells were stained with DiO (green fluorescence), while dead cells were stained with propidium iodide (PI, red fluorescence). As shown in Figure 2h, most of cells were apoptotic/dead (red fluorescence) after treatment with CPCI/DOX-NP plus laser irradiation. By sharp contrast, significant amounts of living cells (green fluorescence) could still be observed in other control groups. We further determined the combination therapeutic effect by calculating the combination index. The results displayed excellent synergistic effect to kill tumor cells between DOX and CPCI-NP+light with

increasing DOX and CPCI-NP concentrations (Figure 2i,j).[46, 47] Annexin FITC/PI assay also revealed synergetic actions on OSC-3 cells resulting in enhancement of cell apoptosis. As shown in Figure S9, CPCI/DOX-NP without laser irradiation and CPCI-NP with laser irradiation were able to lead to 25.39% and 24.31% apoptotic cells, respectively. This percentage further increased to 54.1% when CPCI/DOX-NP was used in combination with laser irradiation.

After demonstrating the *in vitro* synergistic function of CPCI/DOX-NP plus 808 nm laser irradiation, we would like to evaluate its efficacy in the tumor models in mice. First, potential toxicology of CPCI-NP *in vivo* was investigated. As shown in Figure S10 and S11, the assay of complete blood pane and liver function tests all revealed almost normal or no obvious toxicities. We therefore can conclude that CPCI-NP is a highly biocompatible photothermal conversion nano-agent with no significant side effects on mice. Since CPCI-NP is cross-linked by disulfide bonds, we expect it to be relatively stable during circulation. Pharmacokinetics studies comparing free ICG, ICG and TBAI co-encapsulated by PCLC telodendrimer (PCLC/TBAI&ICG-NP), and CPCI-NP were performed in female Sprague–Dawley rats. As shown in Figure 3a, hydrophilic free ICG quickly diffused into tissue and was cleared from circulation within 30 min after intravenous injection ($t_{1/2}$ = 5.22 min; AUC = 12.091 mg/L*h). 48 h after injection, the dose of ICG from PCLC/TBAI&ICG NPs in blood was found to decrease to 9.4% injected dose per gram of tissue (%ID g^{-1}) ($t_{1/2}$ = 28.421 h; AUC = 677.571 mg/L*h). In contrast, about 20.4% ID g^{-1} of ICGD from CPCI-NP was still in blood circulation ($t_{1/2}$ = 41.098 h; AUC = 1196.274 mg/L*h), indicating high stability of ICGD and CPCI-NP.

Due to its relatively small size, reversibly crosslinking nature and unique architecture-dependent near-infrared fluorescence property, CPCI/DOX-NP is particularly suitable for use as activatable optical nanoprobes for improved cancer detection, preferential accumulation and signal amplification at the tumor tissue.[48, 49] As shown in Figure 3b, the near infrared fluorescent imaging of nude mice bearing orthotopic OSC-3 oral cancer after intravenous injection of CPCI/DOX-NP. Fluorescent signal of ICGD at the tumor site (indicated by green fluorescent protein, GFP) was found to be time-dependent and peaked at 36 h after injection (Figure 3c). The intense fluorescence at the tumor sites showed no obvious decay even at 48 h after injection, implying a persistent tumor accumulation of CPCI/DOX-NP, which meant a wide time window for initiating phototherapy *in vivo.* Semi-quantitative fluorescence biodistribution based on *ex vivo* imaging of major organs and tumor indicated the high tumor uptake of CPCI/DOX-NP (Figure 3d,f). Meanwhile, tumor tissue slice was observed that highly coincident fluorescent signals of ICGD (green color) and DOX (red color) concurrently appeared in the tumor regions (Figure 3e).

The tissue distribution of DOX over time after tail vein administration of CPCI/DOX-NP was determined. At 24 h, 48 h and 5 d after injection, DOX concentrations in tumor and normal organs were measured by high pressure liquid chromatography-mass spectroscopy (HPLC-MS). As shown in Figure 3g, accumulation of DOX in the tumor, liver and even kidney were noted at 24 h. However, accumulation concentration of DOX in liver and kidney were rapidly cleared with the passage of time, especially after 5 days. It was gratifying to see that DOX concentration at the tumor site remained at about 2 μg per g tissue after 5

days, which could explain its anti-tumor efficacy shown below. DOX is commonly used to treat many different types of cancers; cardiotoxicity and myelosuppression are the dose limiting toxic side effects for this very important drug.[50] Fortunately, according to Figure 3f,g, fluorescence intensity of ICGD and concentration of DOX in the heart were extremely low, indicating low accumulation of CPCI/DOX-NP and low DOX release in the heart. This very important attribute is needed for future successful clinical applications of our CPCI/DOX-NP.

Encouraged by the *in vitro* anti-tumor activity and *in vivo* favorable biodistribution and of CPCI/DOX-NP system, we investigated therapeutic efficacy in nude mice bearing orthotopic OSC-3 cells oral cancer. First, photothermal conversion effect of CPCI/DOX-NP in the tumor site of nude mice was investigated. 24 h after systemic administration of PBS, PCI-NP, CPCI-NP or CPCI/DOX-NP, the tumor region in living mice was irradiated by 808 nm laser (0.8 W cm^{-2} for 2 min). As shown in Figure 4a, b, the mean temperature of tumor region for both CPCI-NP and CPCI/DOX-NP groups was found to increase by about 50 °C, which was about 1.37-fold and 8.92-fold higher than that of PCI-NP group ($\Delta T \approx 36.5$ °C) and PBS group ($\Delta T \approx 5.6$ °C). Such high increase in temperature was more than sufficient to cause irreversible damage to cancer cells.[51] It is noteworthy that it still took a short time (45 seconds) for CPCI-NP or CPCI/DOX-NP groups to rapidly heat up more than 40 °C, which was in accordance with the fast heating rate observed in the *in vitro* studies.

Mice were randomly divided into five groups: (1) PBS, (2) free DOX, (3) PCI-NP, (4) CPCI-NP and (5) CPCI/DOX-NP. Near infrared laser irradiation (808nm, 0.8 W cm^{-2} for 2 min) was used in all groups. The treatment conceive was shown in Figure 4c. When tumor volume reached about 100 mm^3, CPCI/DOX-NP was injected *via* tail intravenous, and then tumor site was irradiated by laser at 24 h and 48 h after injection (*i.e.* day 2 and 3). Afterwards, the same treatment regimen (photothermal agent followed by light irradiation) was repeated on day 7, 8 and 9. As shown in Figure 4d, PCI-NP group, CPCI-NP group and CPCI/DOX-NP group displayed satisfactory antitumor effect in the first 10 days of treatment. However, for both the PCI-NP and CPCI-NP groups, tumor began to regrow at the primary site. In contrast, complete tumor remission was achieved in the animals receiving CPCI/DOX-NP plus laser irradiation, validating synergistic therapeutic efficacy of combination photothermal/chemo-therapy. Figure 4e shows representative photographs of a mouse treated with CPCI/DOX-NP plus laser irradiation. No palpable tumor was found at day 28. In addition, no significant change in body weights was observed after the treatments (Figure S12). The histological analysis further confirmed that most tumor cells were destroyed after one cycle of treatment, with much lower level of nuclear polymorphism and less cancer cell density in tumor sections than those of other treatment groups (Figure S13).

The aforementioned experimental results clearly demonstrate that CPCI/DOX-NP is a highly efficacious phototherapeutic system for local therapy where the treatment region is accessible to light. However, cancers are often accompanied by recurrence and metastasis. In the last few years, immunotherapy with check-point blockade antibodies has been proven to be clinically very promising, although the response rate varies greatly among different tumors types. Imiquimod is an immune response modifier that binds to toll-like receptor 7, and it has been approved by the U.S. Food and Drug Administration (FDA) for topical

treatment of genital warts, superficial basal cell carcinoma and actinic keratosis. However, it is too toxic to be given systemically.[52] Owing to the excellent encapsulating ability of CPCI-NP, imiquimod can be loaded into the core of CPCI-NP with extremely high drug encapsulating capacity, while keeping a desirable nanoparticle size of 22 ± 4 nm for preferential tumor accumulation (Figure S14 and 15). We investigated if photothermal/immunotherapy based on our CPCI/imiquimod-NP, in combination with PD-1 check point blockade therapy, could enhance the anticancer synergistic immunotherapeutic efficacy against metastatic tumors (Figure 5a).

The treatment conceive was shown in Figure 5b. An artificial mimic of metastasis tumor (bilateral breast tumor model) was developed by orthotopically injecting syngeneic 4T1 breast cancer cells into both the left and right mammary fat pad of the same immunocompetent mouse. The right tumor was designated as the primary tumor to be treated by laser and the left tumor was inoculated as a distant tumor or "metastatic" tumor without light treatment. Mice were randomly divided into seven groups: (1) PBS (untreated); (2) CPCI/imiquimod-NP for 2 cycles treatment; (3) CPCI-NP combining laser irradiation for 2 cycles treatment; (4) CPCI/imiquimod-NP combining laser irradiation for 2 cycles treatment; (5) CPCI/imiquimod-NP plus monoclonal antibody (α-PD-1) for 2 cycles treatment; (6) CPCI/imiquimod-NP combining laser irradiation plus α-PD-1 for 1 cycle treatment; (7) CPCI/imiquimod-NP combining laser irradiation plus α-PD-1 for 2 cycles treatment. For group 7, when tumor volume reached about 50 mm^3, CPCI/imiquimod-NP was injected intravenously. 24 h later, the primary tumor was locally exposed to 808 nm laser irradiation for 2 min (0.8 W cm^{-2}). Afterwards, mice were intraperitoneally (i.p.) injected with α-PD-1 at doses of 200 μg per mouse on day 2. Subsequently, second cycle administrations (i.v. injection of CPCI/imiquimod-NP, tumor local laser irradiation and i.p. injection of α-PD-1) were repeated one time on day 6, 7 and 8. As shown in Figure 5c, the primary tumors of all groups locally irradiated with laser were almost eliminated by CPCI-NP-based early stages photothermal therapy. Due to the lack of further treatment such as second laser irradiation or the absent of imiquimod or α-PD-1 immunity effect, tumor recurrence did occur at control groups 3, 4 and 6 after day 8. It's worth noting that group 5 (CPCI/imiquimod-NP plus α-PD-1) showed inhibition of the growth of primary tumors to some extent, but was not able to eliminate the tumor without laser irradiation. In strike contrast, the combination treatment (group 7) could significantly eliminate primary tumors without recurrence, indicating that such non-specific combination photothermal/immuno-therapy was highly efficacious against primary tumor.

Not unexpected, we have also observed that mice with their primary tumors ablated by laser could delay the growth of distant non-irradiated tumors (Figure 5d). This is especially true for group 7, in which the distant tumors showed almost complete disappearance, achieving efficacies much better than that obtained in group 5 (without PTT of primary tumors). This encouraging data verified that PTT of primary tumor could elicit an obvious inhibitory effect on distant tumor. Representative photographs of primary and distant tumors in one mouse from group 7 over time are shown in Figure 5e, which clearly show the abscopal effect. As another control, the immunological response induced in group 3 was much better than that in group 4 (without imiquimod), demonstrating the important role of imiquimod to trigger strong immune responses. Last but not least, though primary tumors were treated by laser,

the immunological response induced by group 4 (without α-PD-1) or group 6 (1 cycle of α-PD-1) could only inhibit the growth of distant tumors in the earlier time points, revealing α-PD-1 blockade treatment strategy did play a central role in continually killing tumor cells *via* activating T cells to recognize tumor cells. Overall, the survival curves correlate well with tumor growth results (Figure S16). All animals receiving PBS died within 36 days, whereas 66.7% of animals in group 7 receiving combination nano-photo-immunotherapy survived more than 66 days.

We further investigated the mechanism of synergistic anti-tumor effect triggered by CPCI/imiquimod-NP-based PTT combining with α-PD-1 therapy. In these experiments, mice were divided into four groups for one cycle of treatment (group 1: PBS; groups 2: CPCI/imiquimod-NP; group 3; CPCI/imiquimod-NP plus laser irradiation; group 4: CPCI/imiquimod-NP plus laser irradiation plus α-PD-1). Treated mice were sacrificed and residual tumors from both sides were collected for assessment by H&E staining, RT-PCR and IHC. H&E staining directly displayed large areas of primary tumor cellular destruction and apoptosis in group 3 and 4, and distant tumors also shrunk because of systemic immunotherapeutic effect response, which was in obvious contrast to control group 1 and 2 (Figure S17). Imiquimod can activate natural killer cells, macrophages and B-lymphocytes *via* TLR-7 secrete cytokines (IFN-α, IL-6 and TNF-α) to further enhance activation of the immune response. We therefore evaluated IFN-α, TNF-α, IL4, IL6 (cellular immune related markers), and IL-12 (innate immune marker) gene expression *via* RT-PCR. As shown in Figure 5f, the relative expression of these immune markers in primary tumor treated with laser irradiation was higher than that without laser irradiation, which verified that PTT could induce strong tumor-specific immune responses by producing tumor-associate antigens from ablated tumor cell residues. In addition, the relative expressions of these immune markers in the distant tumors demonstrate the importance of light irradiation of primary tumors (group 3 and 4). Cytotoxic T lymphocytes ($CD8^+$) could directly kill targeted cancer cells, and meanwhile $CD3^+$ and $CD4^+$ helper T cells could also play important roles in the regulation of adaptive immunities. We verified expression of these proteins ($CD8^+$, $CD3^+$, $CD4^+$, PD-1 and PD-L1) on tumors on both sides. As shown in Figure S18, tumor cell numbers in treated primary tumors (group 3 and 4) appeared significantly less, due to the cytotoxic effects of PTT treatment. In addition, much more $CD8^+$, $CD3^+$, $CD4^+$ and PD-1 T cells in distant tumors were found in group 3 and 4 (combination imiquimod and light treatment group) than that in PBS and imiquimod only groups. Meanwhile, we also investigated dendritic cells (DC) maturation. As shown in Figure S19, more MHC II and CD11b expression were found in the primary and distant tissue of animals in group 3 and 4 than in PBS and imiquimod only groups. These results clearly demonstrate that systemic administration of CPCI/imiquimod-NP and α-PD-1 checkpoint blockade antibody, in conjunction with local PTT are highly efficacious against local as well as distant metastatic tumors. This therapeutic concept is highly translatable and can be readily tested in clinical trial.

To evaluate the immune memory induced by CPCI/Imiquimod-based PTT combining α-PD-1, “cured mice” from group 7 of Figure 5 were implanted subcutaneously (left and right lower ventral areas) with 4T1 tumor cells on day 66, followed by i.p. injection of α-PD-1 antibody on day 67 and day 73 (200 μg per mouse each time) (Figure S20a). As negative control, naïve nude mice of the same age were used. Tumor growth of the implanted tumors

was followed. The result is shown in Figure S20b,c, which clearly demonstrate the immune memory effect (significant delay in tumor growth) present in mice previously treated successfully with photothermal/immuno-therapy. The tumor volume increased rapidly in the previously untreated control group even with the injection of α-PD-1.

In summary, the new generation of PTCA based on co-assembled binary telodendrimers (CPCI-NP nanoplatform) was found to exhibit superior photothermal conversion efficiency, heating capability and *in vivo* stability for photothermal therapy. We have demonstrated its utility as (1) a versatile chemo-nanoplatform for synergistic photothermal/chemo-therapy against orthotopic oral cancer, and (2) a immuno-nanoplatform for synergistic photothermal/immuno-therapy against metastatic breast cancer. This highly promising nanoplatform shows enormous potential for clinical translation against many different tumor types, under various clinical scenarios. Although not emphasized above, we envision that CPCI/imiquimod-NP or CPCI/doxorubicin-NP can also be used as a convenient tumor targeting near infrared fluorescent probe for image-guided surgery, followed by intra-operative PTT of the surgical bed. For patients with unresectable or metastatic tumors, including the deadly glioblastoma, selected tumor sites can be irradiated with light *via* optical fiber 24 hr after i.v. administration of CPCI/imiquimod-NP. We envision that this additional nano-photo-immunotherapy will greatly increase the response rate of patients undergoing check point blockade immunotherapy. It is expected that their efficacy could be further improved by introducing tumor targeting ligands or blood brain barrier penetration ligands to the nanocarriers.[53]

Supplementary Material

Refer to Web version on PubMed Central for supplementary material.

ACKNOWLEDGMENTS

This work was supported in part by NIH/NCI grants (R01CA115483, U01CA198880, R01CA199668 and R01CA232845), NIH/NIBIB grant (R01EB012569) and NIH/NICHD grant (R01HD086195).

REFERENCES

(1). Shuhendler AJ; Pu K; Cui L; Uetrecht JP; Rao J Real-time imaging of oxidative and nitrosative stress in the liver of live animals for drug-toxicity testing. Nat. Biotechnol 2014, 32 (4), 373–380. [PubMed: 24658645]

(2). Li YP; Lin TY; Luo Y; Liu QQ; Xiao WW; Guo WC; Lac D; Zhang HY; Feng CH; Wachsmann-Hogiu S; Walton JH; Cherry SR; Rowland DJ; Kukis D; Pan CX; Lam KS A smart and versatile theranostic nanomedicine platform based on nanoporphyrin. Nat. Commun 2014, 5, 4712. [PubMed: 25158161]

(3). Wang S; Lin J; Wang Z; Zhou Z; Bai R; Lu N; Liu Y; Fu X; Jacobson O; Fan W; Qu J; Chen S; Wang T; Huang P; Chen X Core-Satellite Polydopamine-Gadolinium-Metallofullerene Nanotheranostics for Multimodal Imaging Guided Combination Cancer Therapy. Adv. Mater 2017, 29 (35), 170013.

(4). Chen W; Zeng K; Liu H; Ouyang J; Wang L; Liu Y; Wang H; Deng L; Liu Y-N Cell Membrane Camouflaged Hollow Prussian Blue Nanoparticles for Synergistic Photothermal-/Chemotherapy of Cancer. Adv. Funct. Mater 2017, 27 (11), 1605795.

(5). Qi J; Fang Y; Kwok RTK; Zhang X; Hu X; Lam JWY; Ding D; Tang BZ Highly Stable Organic Small Molecular Nanoparticles as an Advanced and Biocompatible Phototheranostic Agent of Tumor in Living Mice. ACS Nano 2017, 11 (7), 7177–7188. [PubMed: 28692799]

(6). Guo W; Guo CS; Zheng NN; Sun TD; Liu SQ CsxWO3 Nanorods Coated with Polyelectrolyte Multilayers as a Multifunctional Nanomaterial for Bimodal ImagingGuided Photothermal/ Photodynamic Cancer Treatment. Adv. Mater 2017, 29 (4), 1601157.

(7). Song C; Blaber MG; Zhao G; Zhang P; Fry HC; Schatz GC; Rosi NL Tailorable plasmonic circular dichroism properties of helical nanoparticle superstructures. Nano Lett. 2013, 13 (7), 3256–3261. [PubMed: 23777529]

(8). Jiang Y; Cui D; Fang Y; Zhen X; Upputuri PK; Pramanik M; Ding D; Pu K Amphiphilic semiconducting polymer as multifunctional nanocarrier for fluorescence/photoacoustic imaging guided chemo-photothermal therapy. Biomaterials 2017, 145, 168–177. [PubMed: 28866477]

(9). Kumar A; Kumar S; Rhim WK; Kim GH; Nam JM Oxidative nanopeeling chemistry-based synthesis and photodynamic and photothermal therapeutic applications of plasmonic core-petal nanostructures. J. Am. Chem. Soc 2014, 136 (46), 16317–1625. [PubMed: 25386786]

(10). Chen Q; Xu LG; Liang C; Wang C; Peng R; Liu Z Photothermal therapy with immune-adjuvant nanoparticles together with checkpoint blockade for effective cancer immunotherapy. Nat. Commun 2016, 7, 13193. [PubMed: 27767031]

(11). Gao F; Sun M; Xu L; Liu L; Kuang H; Xu C Biocompatible Cup-Shaped Nanocrystal with Ultrahigh Photothermal Efficiency as Tumor Therapeutic Agent. Adv. Funct. Mater 2017, 27 (24) 1700605.

(12). Lyu Y; Xie C; Chechetka SA; Miyako E; Pu K Semiconducting Polymer Nanobioconjugates for Targeted Photothermal Activation of Neurons. J. Am. Chem. Soc 2016, 138 (29), 9049–9052. [PubMed: 27404507]

(13). Jiang Y; Pu K Advanced Photoacoustic Imaging Applications of Near-Infrared Absorbing Organic Nanoparticles. Small 2017, 13 (30) 1700710.

(14). Yao C; Wang P; Li X; Hu X; Hou J; Wang L; Zhang F Near-Infrared-Triggered Azobenzene-Liposome/Upconversion Nanoparticle Hybrid Vesicles for Remotely Controlled Drug Delivery to Overcome Cancer Multidrug Resistance. Adv. Mater 2016, 28 (42), 9341–9348. [PubMed: 27578301]

(15). Xu R; Zhang G; Mai J; Deng X; Segura-Ibarra V; Wu S; Shen J; Liu H; Hu Z; Chen L; Huang Y; Koay E; Huang Y; Liu J; Ensor JE; Blanco E; Liu X; Ferrari M; Shen H An injectable nanoparticle generator enhances delivery of cancer therapeutics. Nat. Biotechnol 2016, 34 (4), 414–418. [PubMed: 26974511]

(16). Zhang P; Wang Y; Lian J; Shen Q; Wang C; Ma B; Zhang Y; Xu T; Li J; Shao Y; Xu F; Zhu JJ Engineering the Surface of Smart Nanocarriers Using a pH-/Thermal-/GSH-Responsive Polymer Zipper for Precise Tumor Targeting Therapy *In Vivo*. Adv. Mater 2017, 29 (36), 1702311.

(17). Deng X; Li K; Cai X; Liu B; Wei Y; Deng K; Xie Z; Wu Z; Ma P; Hou Z; Cheng Z; Lin J Hollow-Structured CuS@Cu_2S@Au Nanohybrid: Synergistically Enhanced Photothermal Efficiency and Photoswitchable Targeting Effect for Cancer Theranostics. Adv. Mater 2017, 29 (36), 1701266.

(18). Lin TY; Li YP; Liu QQ; Chen JL; Zhang HY; Lac D; Zhang H; Ferrara KW; Wachsmann-Hogiu S; Li TH; Airhart S; White RD; Lam KS; Pan CX Novel theranostic nanoporphyrins for photodynamic diagnosis and trimodal therapy for bladder cancer. Biomaterials 2016, 104, 339–351. [PubMed: 27479049]

(19). Duan X; Chan C; Guo N; Han W; Weichselbaum RR; Lin W Photodynamic Therapy Mediated by Nontoxic Core-Shell Nanoparticles Synergizes with Immune Checkpoint Blockade To Elicit Antitumor Immunity and Antimetastatic Effect on Breast Cancer. J. Am. Chem. Soc 2016, 138 (51), 16686–16695. [PubMed: 27976881]

(20). Yang G; Xu L; Chao Y; Xu J; Sun X; Wu Y; Peng R; Liu Z Hollow MnO_2 as a tumor-microenvironment-responsive biodegradable nano-platform for combination therapy favoring antitumor immune responses. Nat. Commun 2017, 8 (1), 902. [PubMed: 29026068]

(21). Gotwals P; Cameron S; Cipolletta D; Cremasco V; Crystal A; Hewes B; Mueller B; Quaratino S; Sabatos-Peyton C; Petruzzelli L; Engelman JA; Dranoff G Prospects for combining targeted and

conventional cancer therapy with immunotherapy. Nat. Rev. Cancer 2017, 17 (4), 286–301. [PubMed: 28338065]

(22). Banchereau J; Palucka K Immunotherapy: Cancer vaccines on the move. Nat. Rev. Clin. Oncol 2016, 15, 9–10.

(23). Bombarely A; Moser M; Amrad A; Bao M; Bapaume L; Barry CS; Bliek M; Boersma MR; Borghi L; Bruggmann R; Bucher M; D'Agostino N; Davies K; Druege U; Dudareva N; Egea-Cortines M; Delledonne M; Fernandez-Pozo N; Franken P; Grandont L; Heslop-Harrison JS; Hintzsche J; Johns M; Koes R; Lv X; Lyons E; Malla D; Martinoia E; Mattson NS; Morel P; Mueller LA; Muhlemann J; Nouri E; Passeri V; Pezzotti M; Qi Q; Reinhardt D; Rich M; Richert-Poggeler KR; Robbins TP; Schatz MC; Schranz ME; Schuurink RC; Schwarzacher T; Spelt K; Tang H; Urbanus SL; Vandenbussche M; Vijverberg K; Villarino GH; Warner RM; Weiss J; Yue Z; Zethof J; Quattrocchio F; Sims TL; Kuhlemeier C Insight into the evolution of the Solanaceae from the parental genomes of Petunia hybrida. Nat Plants 2016, 2 (6), 16074. [PubMed: 27255838]

(24). Nagarsheth N; Wicha MS; Zou W Chemokines in the cancer microenvironment and their relevance in cancer immunotherapy. Nat. Rev. Immunol 2017, 17 (9), 559–572. [PubMed: 28555670]

(25). Chen Y; Xia R; Huang Y; Zhao W; Li J; Zhang X; Wang P; Venkataramanan R; Fan J; Xie W; Ma X; Lu B; Li S An immunostimulatory dual-functional nanocarrier that improves cancer immunochemotherapy. Nat. Commun 2016, 7, 13443. [PubMed: 27819653]

(26). Lu J; Liu X; Liao YP; Salazar F; Sun B; Jiang W; Chang CH; Jiang J; Wang X; Wu AM; Meng H; Nel AE Nano-enabled pancreas cancer immunotherapy using immunogenic cell death and reversing immunosuppression. Nat. Commun 2017, 8 (1), 1811. [PubMed: 29180759]

(27). He C; Duan X; Guo N; Chan C; Poon C; Weichselbaum RR; Lin W Core-shell nanoscale coordination polymers combine chemotherapy and photodynamic therapy to potentiate checkpoint blockade cancer immunotherapy. Nat. Commun 2016, 7, 12499. [PubMed: 27530650]

(28). Hugo W; Zaretsky JM; Sun L; Song C; Moreno BH; Hu-Lieskovan S; Berent-Maoz B; Pang J; Chmielowski B; Cherry G; Seja E; Lomeli S; Kong X; Kelley MC; Sosman JA; Johnson DB; Ribas A; Lo RS Genomic and Transcriptomic Features of Response to Anti-PD-1 Therapy in Metastatic Melanoma. Cell 2016, 165 (1), 35–44. [PubMed: 26997480]

(29). Bu X; Mahoney KM; Freeman GJ Learning from PD-1 Resistance: New Combination Strategies. Trends Mol. Med 2016, 22 (6), 448–451. [PubMed: 27174038]

(30). Sharpe AH Introduction to checkpoint inhibitors and cancer immunotherapy. Immunol. Rev 2017, 276 (1), 5–8. [PubMed: 28258698]

(31). Guo LR; Yan DD; Yang DF; Li YJ; Wang XD; Zalewski O; Yan BF; Lu W Combinatorial Photothermal and Immuno Cancer Therapy Using Chitosan-Coated Hollow Copper Sulfide Nanoparticles. ACS Nano 2014, 8 (6), 5670–5681. [PubMed: 24801008]

(32). Tao Y; Ju E; Ren J; Qu X Immunostimulatory oligonucleotides-loaded cationic graphene oxide with photothermally enhanced immunogenicity for photothermal/immune cancer therapy. Biomaterials 2014, 35 (37), 9963–9971. [PubMed: 25224368]

(33). Kostarelos K; Bianco A; Prato M Promises, facts and challenges for carbon nanotubes in imaging and therapeutics. Nat. Nanotechnol 2009, 4 (10), 627–633. [PubMed: 19809452]

(34). Zhou F; Wu S; Song S; Chen WR; Resasco DE; Xing D Antitumor immunologically modified carbon nanotubes for photothermal therapy. Biomaterials 2012, 33 (11), 3235–3242. [PubMed: 22296829]

(35). Li X; Naylor MF; Le H; Nordquist RE; Teague TK; Howard CA; Murray C; Chen WR Clinical effects of in situ photoimmunotherapy on late-stage melanoma patients: a preliminary study. Cancer Biol. Ther. 2010, 10 (11), 1081–1087. [PubMed: 20890121]

(36). Min Y; Roche KC; Tian S; Eblan MJ; McKinnon KP; Caster JM; Chai S; Herring LE; Zhang L; Zhang T; DeSimone JM; Tepper JE; Vincent BG; Serody JS; Wang AZ Antigen-capturing nanoparticles improve the abscopal effect and cancer immunotherapy. Nat. Nanotechnol. 2017, 12 (9), 877–882. [PubMed: 28650437]

(37). Mauldin IS; Wages NA; Stowman AM; Wang E; Olson WC; Deacon DH; Smith KT; Galeassi N; Teague JE; Smolkin ME; Chianese-Bullock KA; Clark RA; Petroni GR; Marincola FM; Mullins DW; Slingluff CL Jr. Topical treatment of melanoma metastases with imiquimod, plus administration of a cancer vaccine, promotes immune signatures in the metastases. Cancer Immunol. Immunother. 2016, 65 (10), 1201–1212. [PubMed: 27522582]

(38). Li YP; Budamagunta MS; Luo JT; Xiao WW; Voss JC; Lam KS Probing of the Assembly Structure and Dynamics within Nanoparticles during Interaction with Blood Proteins. ACS Nano 2012, 6 (11), 9485–9495. [PubMed: 23106540]

(39). Koo AN; Lee HJ; Kim SE; Chang JH; Park C; Kim C; Park JH; Lee SC Disulfide-cross-linked PEG-poly(amino acid)s copolymer micelles for glutathione-mediated intracellular drug delivery. Chem. Commun 2008, 48 (48), 6570–6572.

(40). Wang YC; Black KCL; Luehmann H; Li WY; Zhang Y; Cai X; Wan DH; Liu SY; Li M; Kim P; Li ZY; Wang LV; Liu YJ; Xia YN Comparison Study of Gold Nanohexapods, Nanorods, and Nanocages for Photothermal Cancer Treatment. ACS Nano 2013, 7 (3), 2068–2077. [PubMed: 23383982]

(41). Hessel CM; Pattani VP; Rasch M; Panthani MG; Koo B; Tunnell JW; Korgel BA Copper selenide nanocrystals for photothermal therapy. Nano Lett. 2011, 11 (6), 2560–2566. [PubMed: 21553924]

(42). Fernandez A; Manchanda R; McGoron AJ Theranostic applications of nanomaterials in cancer: drug delivery, image-guided therapy, and multifunctional platforms. Appl. Biochem. Biotechnol 2011, 165 (7-8), 1628–1651. [PubMed: 21947761]

(43). Kim TH; Chen Y; Mount CW; Gombotz WR; Li X; Pun SH Evaluation of temperature-sensitive, indocyanine green-encapsulating micelles for noninvasive near-infrared tumor imaging. Pharm. Res 2010, 27 (9), 1900–1913. [PubMed: 20568000]

(44). Li YP; Xiao K; Luo JT; Xiao WW; Lee JS; Gonik AM; Kato J; Dong TA; Lam KS Well-defined, reversible disulfide cross-linked micelles for on-demand paclitaxel delivery. Biomaterials 2011, 32 (27), 6633–6645. [PubMed: 21658763]

(45). Zhang L; Xiao H; Li JG; Cheng D; Shuai XT Co-delivery of doxorubicin and arsenite with reduction and pH dual-sensitive vesicle for synergistic cancer therapy. Nanoscale 2016, 8, 12608–12617. [PubMed: 26731009]

(46). Chou TC Drug combination studies and their synergy quantification using the Chou-Talalay method. Cancer Res. 2010, 70 (2), 440–446. [PubMed: 20068163]

(47). Chou TC Theoretical basis, experimental design, and computerized simulation of synergism and antagonism in drug combination studies. Pharmacol Rev. 2006, 58 (3), 621–681. [PubMed: 16968952]

(48). Cabral H; Matsumoto Y; Mizuno K; Chen Q; Murakami M; Kimura M; Terada Y; Kano MR; Miyazono K; Uesaka M; Nishiyama N; Kataoka K Accumulation of sub-100 nm polymeric micelles in poorly permeable tumors depends on size. Nat. Nanotechnol 2011, 6 (12), 815–823. [PubMed: 22020122]

(49). Zhang L; Yin T; Li B; Zheng R; Qiu C; Lam KS; Zhang Q; Shuai X Size Modulable Nanoprobe for High-Performance Ultrasound Imaging and Drug Delivery Against Cancer. ACS Nano 2018, 12 (4), 3449–3460. [PubMed: 29634240]

(50). Abdel-Wahab M Influence of p-coumaric acid on doxorubicin-induced oxidative stress in rat's heart. Pharm. Res 2003, 48 (5), 461–465.

(51). Lovell JF; Jin CS; Huynh E; Jin H; Kim C; Rubinstein JL; Chan WCW; Cao W; Wang LV; Zheng G Porphysome nanovesicles generated by porphyrin bilayers for use as multimodal biophotonic contrast agents. Nat. Mater 2011, 10 (4), 324–332. [PubMed: 21423187]

(52). Walter A; Schafer M; Cecconi V; Matter C; Urosevic-Maiwald M; Belloni B; Schonewolf N; Dummer R; Bloch W; Werner S; Beer HD; Knuth A; van den Broek M Aldara activates TLR7-independent immune defence. Nat. Commun 2013, 4, 1560. [PubMed: 23463003]

(53). Liu RW; Li XC; Xiao WW; Lam KS Tumor-targeting peptides from combinatorial libraries. Adv. Drug Deliver. Rev 2017, 110, 13–37.

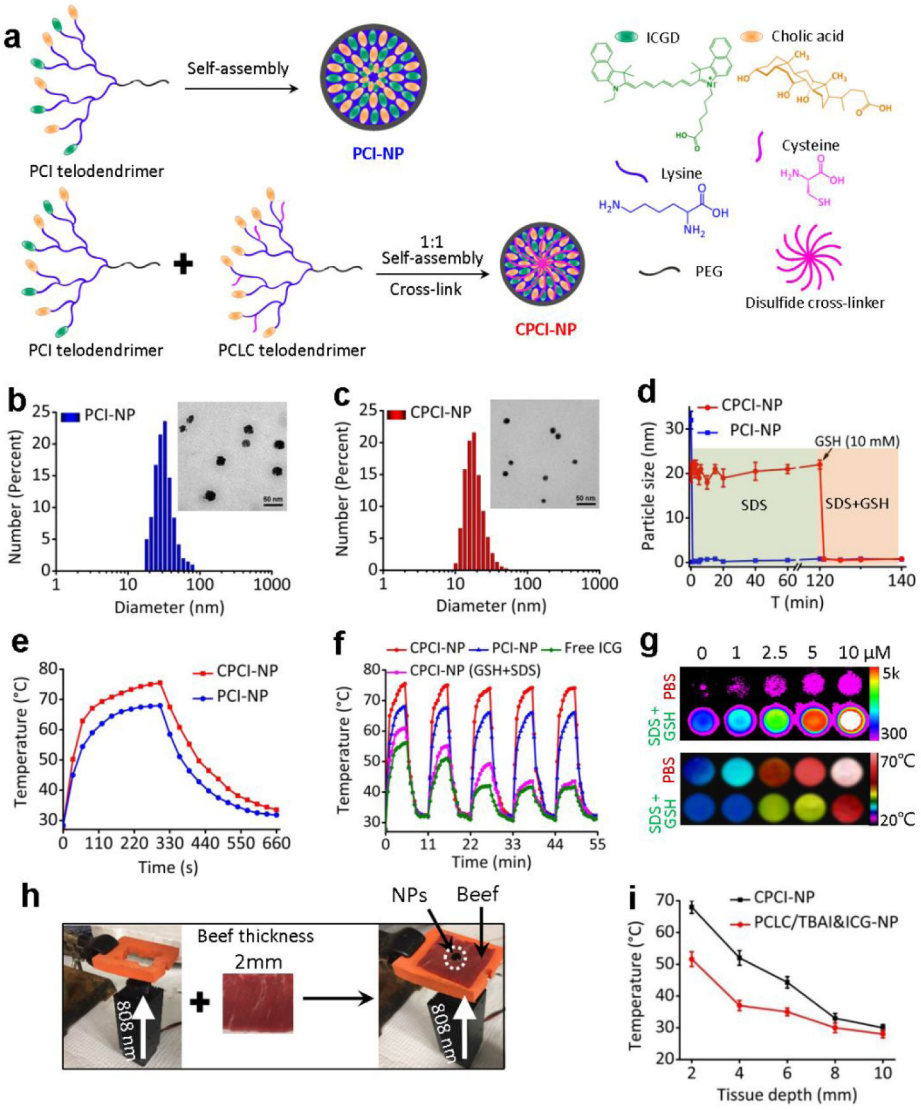

Figure 1.

Design and characterizations of PCI-NP and CPCI-NP. (a) Schematic self-assembly illustration of PCI-NP and CPCI-NP. DLS and TEM imaging of (b) PCI-NP and (c) CPCI-NP PBS solution (stained with uranyl acetate for TEM; telodendrimer concentration: 1 mg mL^{-1}). (d) Continuous dynamic light scattering measurements of PCI-NP and CPCI-NP in SDS for 120 min, after which GSH (10 mM) was added. (e) Comparison of the photothermal conversion behavior of CPCI-NP and PCI-NP under laser irradiation for 300 s. (f) Anti-photobleaching property of CPCI-NP, PCI-NP and ICG in PBS solution, and CPCI-NP in PBS solution with GSH and SDS during five circles of heating-cooling processes. ICGD and ICG concentration: 30 μg mL^{-1}. (g) Near-infrared fluorescence and thermal imaging of CPCI-NP in PBS and GSH+SDS solution at the different concentration. (h) Analogous instrument and (i) temperature variation of CPCI-NP and PCLC/TBAI&ICG-NP under laser irradiation for 30 s to investigate penetration depth and thermal effect. (Laser: 808 nm, 0.8 W cm^{-2})

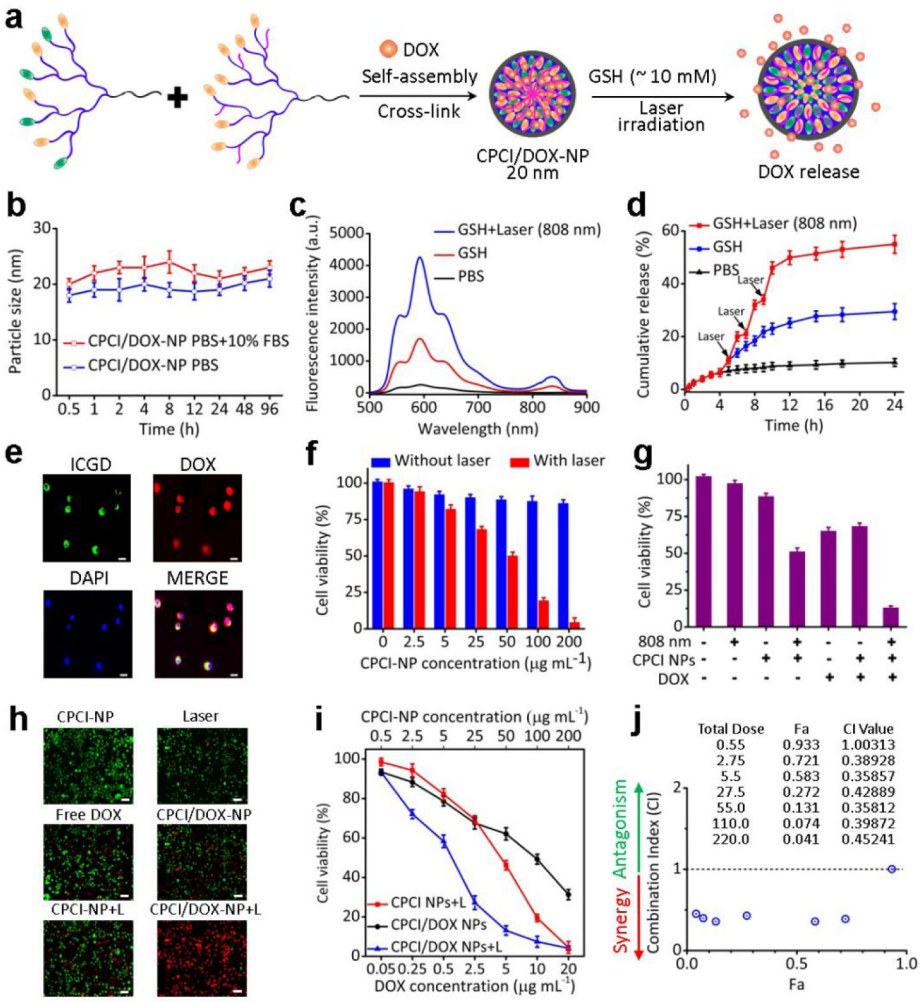

Figure 2.

Characterizations of CPCI/DOX-NP *in vitro* and synergistic cytotoxicity of CPCI/DOX-NP plus 808 nm laser irradiation against OSC-3 oral cancer cells. (a) Schematic self-assembly illustration of CPCI/DOX-NP and DOX release from CPCI/DOX-NP. (b) Serum stability of CPCI/DOX-NP in PBS solution of pH 7.4 with/without 10% FBS was measured by dynamic light scattering (incubation temperature: 37 °C; data were mean ± s.d., $n = 3$). (c) Variation of DOX fluorescence intensity and (d) *in vitro* quantitative DOX release of CPCI/DOX-NP aqueous solution at PBS, GSH (10 mM) and laser (3 times, 2 min each) plus GSH (10 mM) (Data were mean ± s.d., $n = 3$). (e) Uptake of DOX (red) loaded CPCI-NP (green) in OSC-3 oral cancer cell (DOX concentration: 25 μg mL^{-1}; Scale bar = 5 μm). (f) The viability of OSC-3 oral cells incubated with CPCI-NP and CPCI-NP plus laser irradiation at the different concentration ($n = 3$). (g) The viabilities and (h) live/dead staining by DiO/PI of OSC-3 oral cells after different treatments (DOX concentration: 25 μg ML^{-1}; Scale bar = 10 μm). (i) The synergistic treatment effect and (j) combination index (CI) between DOX and CPCI-NP plus laser irradiation for OSC-3 oral cells treatment (The weight ratio of PCI telodendrimer, PCLC telodendrimer and DOX is 10:10:1; CPCI-NP concentration based on PCI telodendrimer; Laser: 808 nm, 0.8 W cm^{-2}; Fa: fraction affected, CI: combination

index, CI value < 1, = 1 and > 1 represent synergy, additive and antagonism effects, respectively).

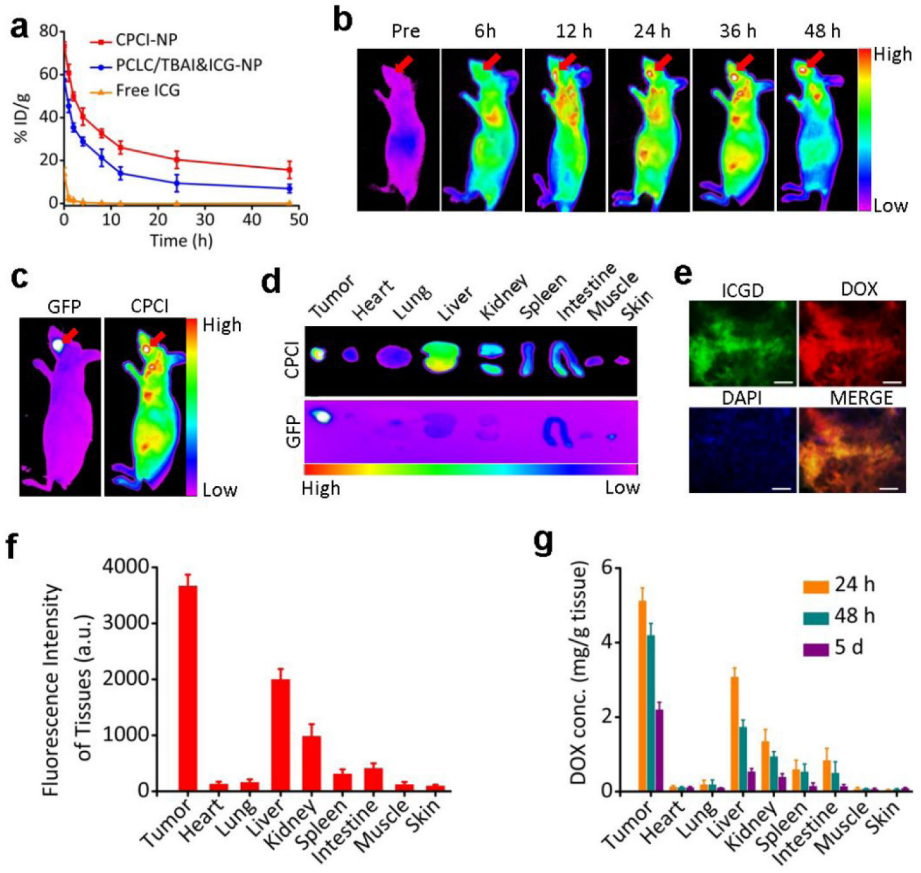

Figure 3.

CPCI/DOX-NP tumor imaging *in vivo.* (a) *In vivo* blood pharmacokinetics of CPCI-NP, PCLC/TBAI&ICG-NP and free ICG at a dose of 5 mg kg^{-1} body weight (Data were mean ± s.d., $n = 3$ for each group). (b) ICGD fluorescence imaging showing tumor accumulation at different time points after tail vein injection and (c) representative *in vivo* imaging of nude mice bearing orthotopic OSC-3 oral cancer labeled by GFP (DOX dose: 2.5 mg kg^{-1}; total telodendrimer dose: 50 mg kg^{-1}; ICGD dose: 7 mg kg^{-1}). The red arrow points to the tumor site. (d) Representative *ex vivo* ICGD fluorescence imaging of the organs and tumor excised at 48 h post-injection time from the same animal. (e) Imaging of the distribution of CPCI/DOX-NP in OSC-3 tumor tissue at 48 h after injection (Red: DOX, Green: ICGD, scale bar = 25 μm). (f) Quantitative analysis of ICGD fluorescence signal intensity inside organs and tumor at 48 h post injection of CPCI/DOX-NP. (g) DOX distribution in organs and tumors tissues of orthotopic OSC-3 oral cancer mice 24 h, 48 h and 5 d post injection of CPCI/DOX-NP. Dose of DOX: 2.5 mg kg^{-1}; data were mean±s.d., $n = 3$ for each time point.

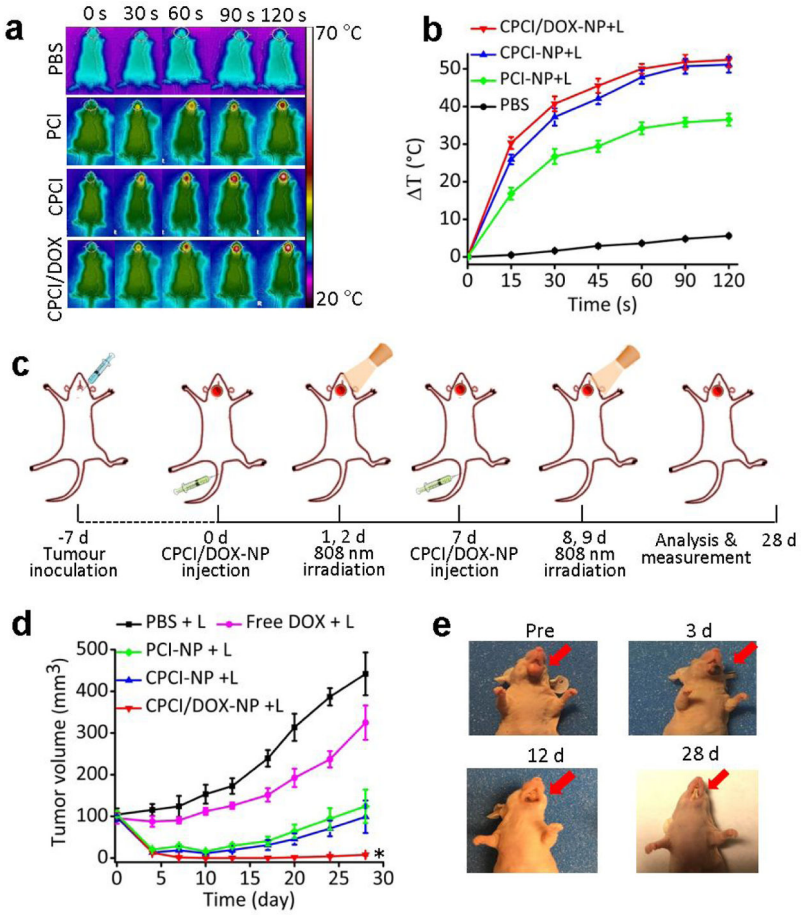

Figure 4.

Synergistic anti-tumor activity of photothermal-/chemotherapy in nude mice bearing orthotopic OSC-3 oral cancer. (a) IR thermal images and (b) mean tumor temperature under 808 nm laser local irradiation (0.8 W cm^{-2}) at 24 h post intravenous administration of PBS, PCI-NP, CPCI-NP, or CPCI/DOX-NP ($n = 3$). (c) Schematic illustration of CPCI/DOX-NP based PTT and chemotherapy to inhibit orthotopic oral tumor growth. (d) Tumor growth curves of mice ($n = 5$ per group) bearing orthotopic OSC-3 oral tumors. (e) Representative photos of tumor volume variation in the group treated by CPCI/DOX-NP plus 808 nm laser. Dose of DOX: 2.5 mg kg^{-1} and ICGD: 7 mg kg^{-1}. *$p < 0.05$ by comparing CPCI/DOX-NP + 808 nm laser irradiation group with control groups. Data are presented as the mean ± s.d..

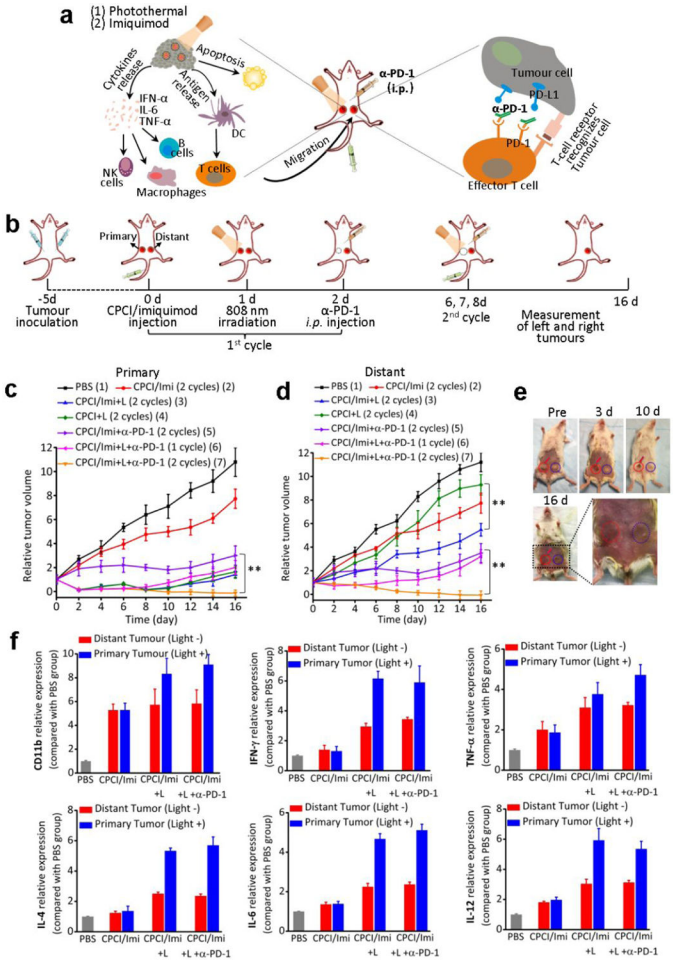

Figure 5.

Synergistic anti-tumor activity of photothermal-/immunotherapy in the mice bearing orthotopic 4T1 breast cancer (both sides). (a) Schematic illustration of the proposed mechanism of anti-tumor immune responses induced by CPCI/Imiquimod-NP in combination with anti-PD-1 therapy. (b) Schematic illustration of synergistic therapy effect of photothermal-/immunotherapy to inhibit tumor growth at primary and distant sites. (c) Primary tumor and (d) distant tumor growth curves of different groups mice bearing 4T1 breast tumors ($n = 6$ per group; dose of imiquimod: 1.25 mg kg^{-1}, total telodendrimer: 50 mg kg^{-1} and ICGD: 7 mg kg^{-1}, intraperitoneal injection of anti-PD-1 200 μg per mouse on day 2 and 8). $^{**}p < 0.01$ in (d) by comparing group 5 (CPCI/Imiquimod-NP + α-PD-1) with group 7 (CPCI/Imiquimod-NP + 808 nm laser + α-PD-1); $^{**}p < 0.01$ in e by comparing group 5 (CPCI/Imiquimod-NP + α-PD-1) with group 7 (CPCI/Imiquimod-NP + 808 nm laser + α-PD-1) and comparing group 4 (CPCI/Imiquimod-NP) with the group 3 (CPCI/Imiquimod-NP + 808 nm laser). (e) Representative photo of tumor volume variation in the mouse treated by CPCI/Imiquimod-NP plus 808 nm laser plus anti-PD-1. The red circle and blue circle shows primary and distant tumor, respectively. (f) The expression of CD11b, IFN-γ, TNF-α, IL-4, IL-6 and IL-12 with different treatments in both sides tumor tissues evaluated by RT-PCR (mean ± s.d., n = 3).

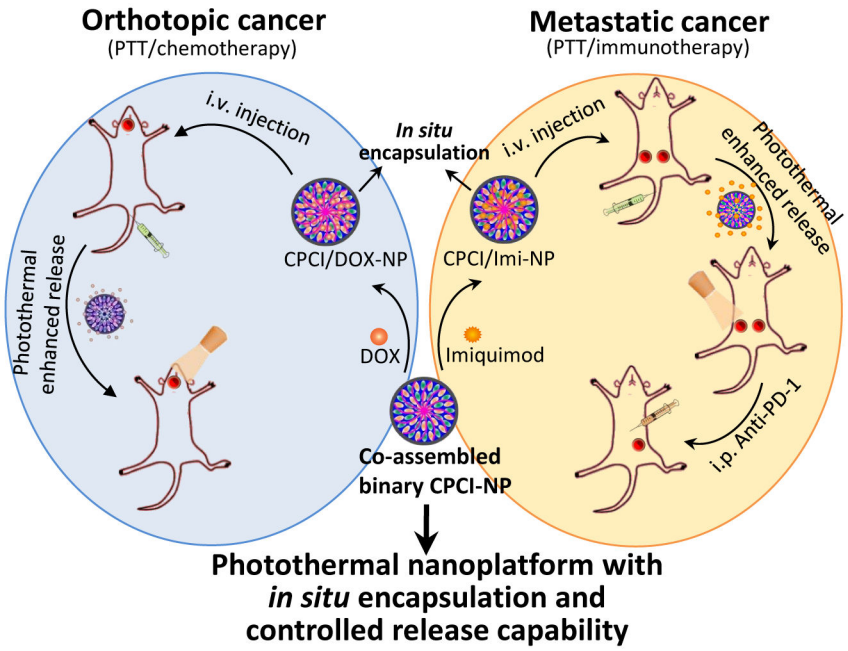

Schema 1.

Schematic illustration of high-performance photothermal nanoparticle (CPCI-NP) with *in situ* encapsulation and controlled release capability of cytotoxic agents and immunomodulatory agents against orthotopic oral cancer and metastatic breast cancer.